A compliant-hull concept for planning craft wave-impact shock reduction

WILLIAM S. VORUS
School of Naval Architecture and Marine Engineering, University of New Orleans, New Orleans, LA 70148, USA

Abstract. The subject of this paper is analysis of high-speed planing-craft wave impact, with the inclusion of hull-surface compliance. The analysis methods were extended in an effort to develop compliant-surface technology for wave-impact shock reduction. The practical outcome of this work, along with experimental cylinder drop-test evaluations, have been reported previously. The overall technology developed is composed of compliant plates over a sub-length of the boat hull. The plates are hinged at the boat keel and supported by vented air bags at the chines. Thus, the required analysis has coupled hydrodynamic, gas-dynamic, and structural-dynamic parts. Only the hydrodynamic part of the complete model is covered here. On the basis of the cylindrical geometry of the drop-test cylinder, two-dimensional theory has been used exclusively. The time history of the distribution of plating deflection predicted from the full analysis is imposed in the free-falling cylinder analysis to demonstrate execution of the hydrodynamic part of the complete coupled theory. The reductions in impact acceleration reported here are therefore the same as determined from the complete analysis.

Key words: high-speed watercraft, hydrodynamics, impact, shock reduction

1. Introduction

The impact of high-speed boats in sea surface waves is the dominant effect limiting the ability of the boat to operate at the desired high speed. Tens of g's of impact acceleration typically occur, resulting in short-term damage to the hull, the equipment, and the human occupants as well. It has therefore been the subject of extensive research for many years, beginning with the benchmark works of von Kármán [1] and Wagner [2].

The modern hydrodynamic model is still based on low-aspect-ratio theory, such that the cross-sections of the vertically impacting craft exhibit approximately two-dimensional flow corresponding to vertically impacting symmetric cylinders.

The theory of Vorus [3] was recently developed for symmetric cylinder-impact analysis, and applies directly to steady, calm water planing of prismatic hulls. The analysis presented here is an extension of the rigid-cylinder impact theory of [3]. The theory of [3] has also provided a sound basis for extension to other configurations, such as dynamic effects of internal sprung mass on impact [4], impact of asymmetric hull forms [5], calm-water planing of non-prismatic hull forms [6–8], planing in rough water [8], multi-hull impact and planing [8].

The extension presented in this paper is to free-fall cylinder impact, where the cylinder bottom plating deflects spatially, in the section, and in time, in an arbitrary, but specified pattern. This theory is required as one part of any analysis aimed at evaluating the benefits of hull compliance on wave-shock impact reduction.

The theory and numerical model for the compliant surface technology development [9], were for the full time-domain hydro-elastic analysis. The analysis there served as the design tool for the 'LocalFlex' shock-reduction system under development, with evaluations from drop-test experiments. In that analysis, with the two-dimensional geometry assumed, the cylinder plating is modeled as an elastic strip-beam hinged at the keel and supported by vented air-bags at the chine. The full theory of that model is not presented here. Instead, the time history of the distribution of plating deflection predicted from the full analysis is imposed on the cylinder plating in free-fall impact to demonstrate execution of the hydrodynamic part of the complete coupled theory. The reductions in impact acceleration reported in [9] are therefore the same as demonstrated here. The impact reduction shown in the following is actually slightly improved over that reported in [9], relative to the experimental predictions, due to refinement of one of the general coupled analysis algorithms.

2. Hydrodynamic theory

Figure 1 below depicts the generalized-cylinder hydrodynamic-impact problem and its mathematical model, following the theory developed in [3]. For this analysis the cylinder geometry is considered, like thin-hydrofoil theory, as a superposition of small normal camber, $\delta(z, t)$, on a nose-tail line at angle $\beta_0(t)$. The height of the contour point (z, t) above the undisturbed waterline is $y_c(z, t)$, as shown on Figure 1:

$$y_c(z, t) = -Y_{wl}(t) + h_c(z, t), \qquad 0 \le z \le z_c(t), \tag{1}$$

with the height above the cylinder keel being:

$$h_c(z, t) = z \, \tan \, \beta_0(t) + \frac{\delta(z, t)}{\cos \, \beta_0(t)}. \tag{2}$$

It is appropriate to note here that $\delta(z, 0)$ need not be zero in the development to follow.

The cylinder falls with velocity $V(t)$ such that the water depth to the keel at any time t is:

$$Y_{wl}(t) = \int_{t_0=0}^{t} V(t_0) \mathrm{d}t_0. \tag{3}$$

$V(t)$, $\beta_0(t)$, and $\delta(z, t)$ in (1) through (3) can be considered as either specified, as is the case here, or to be determined from dynamic force-equilibrium conditions.

By the base theory of Vorus [3], dynamic and kinematic boundary conditions are satisfied with (1) on the z-axis via *geometric* linearization based on small deviation from hull-contour flatness. This is the same asymptotics as that of the early models of [1] and [2], as well as most others implemented since that time, *e.g.* [10], [11], and the asymptotic theory of [12]. The difference in the theory used here is that the *hydrodynamic* nonlinearities are retained in the boundary conditions. This is considered required for mathematical consistency on the basis that, as the cylinder approaches the flatness limit and increasing geometric linearity, the hydrodynamics becomes increasing nonlinear due to the increasing 'squeeze flow' outward from the keel beneath the cylinder. Recognizing and incorporating the two different limits associated with the geometry versus the hydrodynamics is considered to be the most unique feature of the theory of [3].
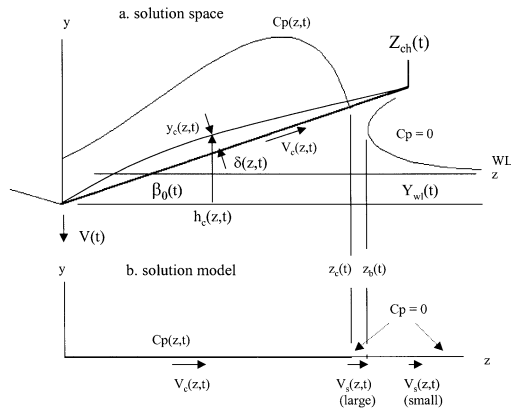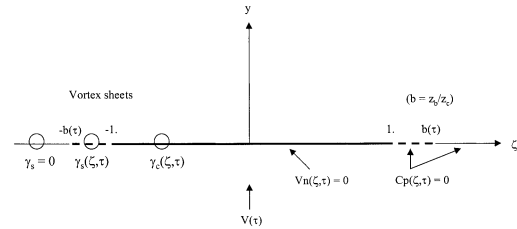
Figure 1. Hydrodynamic model of cylinder impact.　　*Figure 2*. Mathematical model.

The description of Figure 1 is for the so-called 'chine-unwetted' (CUW) flow. Conversely, when the jet-head reaches the chine and the penetration phase of the impact commences, the orders of magnitude of the flow velocities drop abruptly. The impact force also drops abruptly as 'chine-wetting' (CW) occurs, so that this regime is not so important from the standpoint of overall impact reduction.

The model of Figure 1b is in terms of z-axis vortex sheets, Figure 2, where the unknown vortex strengths are the negatives of twice the unknown contour tangential velocities, respectively, by the usual prescription; this is covered in the following development. On Figure 1b, the kinematic boundary condition (KBC) for specified drop-velocity, $V(t)$, and contour height, $h(z, t)$, is satisfied from the keel to the zero pressure point, $z_c(t)$, in terms of the vortex distribution at any time t. The dynamic boundary condition (DBC) of zero pressure is satisfied in the jet-head segment between $z_c(t)$ and $z_b(t)$. Zero pressure is also satisfied trivially on the z-axis beyond the jet-head with an identically zero vortex distribution, as the outward velocity is of higher order there.

For the CUW flow regime depicted on Figure 1, the zero pressure offset lies on the hull normal which tangents the turn of the jet head. The projections to the z-axis provide for the very short free-vortex segment z_c to z_b where zero pressure must be satisfied from the non-linear dynamic-pressure boundary condition. For the subsequent CW flow, $z_c(t)$ is locked to the chine, $z_c(t) = Z_{ch}(t)$, and $z_b(t)$ continues traversing from under the cylinder and outward across the free surface. In that case the free-vortex segment lengthens continually with time from the very short CUW level.

As shown on Figure 2, the z-axis coordinates are scaled on the zero pressure point offset $z_c(t)$ as: $\zeta = z/z_c(\tau)$, $b(\tau) = z_b(\tau)/z_c(\tau)$ and dimensionless time is $\tau = V(0)t/Z_{ch}(0)$, where Z_{ch} is the cylinder chine offset (Figure 1) where transition to CW flow occurs.

The solution of the Figure 1, or Figure 2, model proceeds in a forward time-stepping iteration from the initial wedge similarity solution which occurs first on contacting the water surface. For the CUW flow, Figure 1, for given $V(t)$, $Z_{ch}(t)$, $\beta_0(t)$, and $\delta(z, t)$, the solution unknowns at each time step are $z_c(t)$, $z_b(t)$, and the jet-head separation velocity $V_{s1}(t)$ at $z_c(t)$. For the CW flow there are only two solution unknowns, as $z_c(t) = Z_{ch}(t)$ is known from the cylinder geometry.

The nonlinear solution iteration for the CUW flow proceeds in terms of three conditions: continuity of velocity, continuity of pressure, and continuity of displacement. The CW solution does not require displacement continuity, as the jet-head elevation is not constrained by the presence of a material contour overhead.

As developed from the general solution of the ideal flow boundary-value problem, these continuity conditions are as:

2.1. CONTINUITY OF VELOCITY

Following [3], the contour normal and tangential velocities on Figure 1 in the downward moving coordinate system are:

$$V_n = -h_{c\tau} \cos \beta + (V + v) \cos \beta - w \sin \beta, \quad V_c = -h_{c\tau} \sin \beta + (V + v) \sin \beta + w \cos \beta, \tag{4}$$

where $\beta(\zeta, \tau)$ in (4) is the angle of the local contour tangent:

$$\beta(\zeta, \tau) = \tan^{-1} \frac{\partial}{\partial z} h_c(z, \tau) \qquad \text{at} \quad \zeta = z/z_c(\tau). \tag{5}$$

From (2), $h_{c\tau}$ in (4) is:

$$h_{c\tau} = \frac{\beta_{0\tau}}{\cos^2 \beta_0}(z_c\zeta + \delta \sin \beta_0) + \frac{\delta_\tau}{\cos \beta_0}. \tag{6}$$

Setting $V_n = 0$ in (4), the w velocity component can be eliminated in the contour tangential velocity, leaving:

$$V_c \sin \beta = V + v - h_{c\tau} \equiv v - y_{c\tau}, \tag{7}$$

with $y_{c\tau}$ in (7) from (1).

Define the contour vortex strength as $\gamma_c(z, t)$, such that

$$V_c(\zeta, \tau) = -\frac{1}{2}\gamma_c(\zeta, \tau). \tag{8}$$

Substitute (8) into (7) with the unknowns moved to the left. The resulting kinematic boundary condition is:

$$v(\zeta, \tau) + \frac{1}{2}\gamma_c(\zeta, \tau) \sin \beta(\zeta, \tau) = y_{c\tau}(\zeta, \tau). \tag{9}$$

The vertical velocity, v, in (9) is now written in terms of the vortex distributions by the Biot-Savart law:

$$v(\zeta, \tau) = \frac{1}{2\pi} \int\limits_{\zeta_0=-b(\tau)}^{b(\tau)} \frac{\gamma(\zeta_0, \tau)}{\zeta_0 - \zeta} d\zeta_0. \tag{10}$$

Separate (10) into γ_c and γ_s parts (Figure 2) and implement that γ be an odd function in ζ in the γ_s term. Substitute the result into (9). This produces a Carleman integral equation for the contour vortex distribution, γ_c, in terms of the impact velocity, section geometry, and γ_s on the free sheet, which are all considered as known at any iteration step:

$$\frac{1}{2}\gamma_c(\zeta, \tau)\sin\beta(\zeta, \tau) + \frac{1}{2\pi}\int\limits_{\zeta_0=-1}^{1}\frac{\gamma_c(\zeta_0, \tau)}{\zeta_0 - \zeta}d\zeta_0 = y_{c\tau}(\zeta, \tau) - \frac{1}{\pi}\int\limits_{\zeta_0=1}^{b(\tau)}\frac{\gamma_s(\zeta_0, \tau)\zeta_0}{\zeta_0^2 - \zeta^2}d\zeta_0, \quad (11)$$

$$0 \le \zeta \le 1.$$

The Carleman equation (11) has the following solution, as developed in the Appendix from the theory outlined in [13, Section 81] (the time dependency is to be considered as implicit in the terms of (12) for brevity of notation):

$$\gamma_c(\zeta) = 2\,\cos\widetilde{\beta}(\zeta)\Bigg\{ y_{c\tau}(\zeta)\sin\widetilde{\beta}(\zeta) -$$

$$-\frac{1}{\pi}\frac{\zeta\kappa(\zeta)}{\sqrt{1-\zeta^2}}\Bigg[2\int\limits_{\zeta_0=0}^{1}\frac{y_{c\tau}(\zeta_0)\sqrt{1-\zeta_0^2}\,\cos\widetilde{\beta}(\zeta_0)}{\kappa(\zeta_0)(\zeta_0^2 - \zeta^2)}d\zeta_0 + \int\limits_{\zeta_0=1}^{b}\frac{\gamma_s(\zeta_0)\sqrt{\zeta_0^2-1}}{\kappa(\zeta_0)(\zeta_0^2 - \zeta^2)}d\zeta_0 \Bigg]\Bigg\}. \quad (12)$$

In (12), from the Appendix and [3]:

$$\widetilde{\beta}(\zeta, \tau) \equiv \tan^{-1}[\sin\beta(\zeta, \tau)] \tag{13}$$

and,

$$\kappa(\zeta, \tau) \equiv \prod_{k=1}^{K}\left|\frac{\zeta^2 - \zeta_{k+1}^{*2}}{\zeta^2 - \zeta_k^{*2}}\right|^{\frac{\widetilde{\beta}_k^*(\tau)}{\pi}}. \tag{14}$$

The product function (14) involves the K-element piece-wise linear discretization of the cylinder contour in $0 \le \zeta \le 1$ as shown in Figure 3. The ζ_k^* and $\beta_k^*(\tau)$ are the end offsets and angles of the K linear elements.

The K-discretization is within the general solution of the integral equation, as shown in the Appendix. This is versus the ξ and ζ discretizations to be described in the next section, which are at the boundary-condition level.

First write $y_{c\tau}$ in (12) back in terms of the $V(\tau)$ and $h_{c\tau}(\zeta, \tau)$ components identified in (7) and integrate the $V(\tau)$-terms analytically to achieve:

$$\gamma_c(\zeta) = 2\,\cos\widetilde{\beta}(\zeta)\Bigg\{ h_{c\tau}(\zeta)\sin\widetilde{\beta}(\zeta) -$$

$$-\frac{\zeta\kappa(\zeta)}{\sqrt{1-\zeta^2}}\Bigg[V(\tau) + \frac{2}{\pi}\int\limits_{\zeta_0=0}^{1}\frac{h_{c\tau}(\zeta_0)\sqrt{1-\zeta_0^2}\,\cos\widetilde{\beta}(\zeta_0)}{\kappa(\zeta_0)(\zeta_0^2 - \zeta^2)}d\zeta_0 + \frac{1}{\pi}\int\limits_{\zeta_0=1}^{b}\frac{\gamma_s(\zeta_0)\sqrt{\zeta_0^2-1}}{\kappa(\zeta_0)(\zeta_0^2 - \zeta^2)}d\zeta_0 \Bigg]\Bigg\} \quad (15)$$

Velocity continuity corresponds to removal of the singular terms in (15). For this purpose it is useful to separate the integrands of (15) using the identity:

$$\frac{1}{\zeta_0^2 - \zeta^2} \equiv \frac{1}{\zeta_0^2 - 1}\left(1 + \frac{\zeta^2 - 1}{\zeta_0^2 - \zeta^2}\right). \tag{16}$$
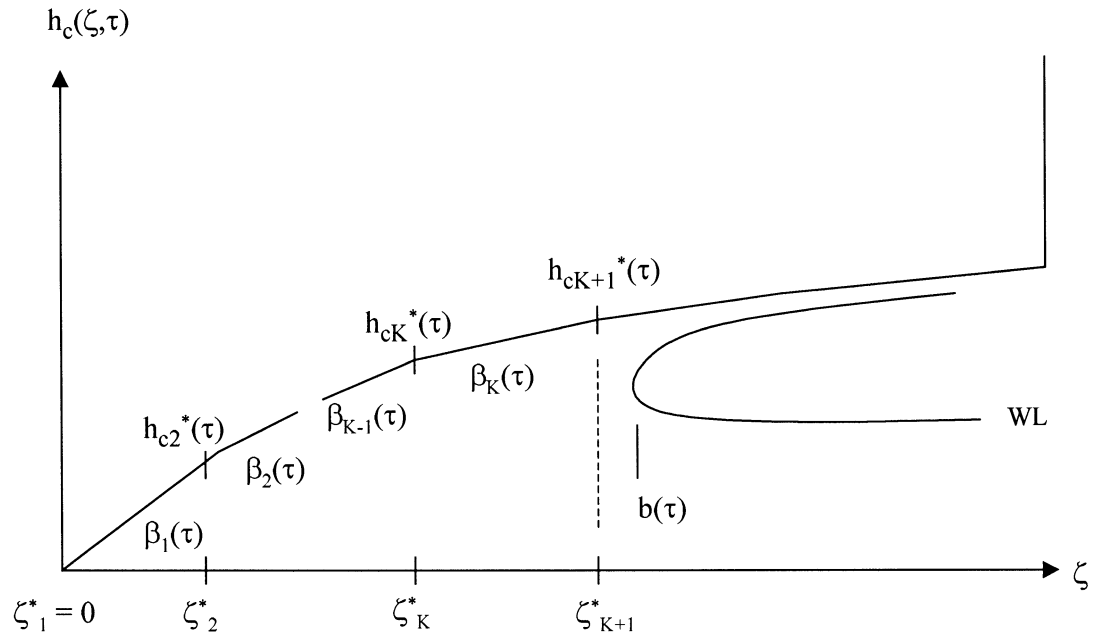
Substitute (16) in (15):

$h_c(\zeta,\tau)$

Figure 3 Contour discretization at time τ.

$$\gamma_c(\zeta) = 2 \, \cos \, \widetilde{\beta}(\zeta) \left\{ h_{c\tau}(\zeta) \sin \widetilde{\beta}(\zeta) - \right. \tag{17}$$

$$-\zeta\kappa(\zeta)\left[\frac{1}{\sqrt{1-\zeta^2}}\left(V(\tau) - \frac{2}{\pi}\int\limits_{\zeta_0=0}^{1}\frac{h_{c\tau}(\zeta_0)\cos\widetilde{\beta}(\zeta_0)}{\kappa(\zeta_0)\sqrt{1-\zeta_0^2}}d\zeta_0 + \frac{1}{\pi}\int\limits_{\zeta_0=1}^{b}\frac{\gamma_s(\zeta_0)}{\kappa(\zeta_0)\sqrt{\zeta_0^2-1}}d\zeta_0\right) + $$

$$\left. \left. +\sqrt{1-\zeta^2}\left(\frac{2}{\pi}\int\limits_{\zeta_0=0}^{1}\frac{h_{c\tau}(\zeta_0)\cos\widetilde{\beta}(\zeta_0)}{\kappa(\zeta_0)\sqrt{1-\zeta_0^2}(\zeta_0^2-\zeta^2)}d\zeta - \frac{1}{\pi}\int\limits_{\zeta_0=1}^{b}\frac{\gamma_s(\zeta_0)}{\kappa(\zeta_0)\sqrt{\zeta_0^2-1}(\zeta_0^2-\zeta^2)}d\zeta_0\right)\right]\right\}.$$

A continuous velocity from the cylinder contour onto the free sheet at $\zeta = 1$ therefore requires, from (17):

$$V(\tau) - \frac{2}{\pi}\int\limits_{\zeta_0=0}^{1}\frac{h_{c\tau}(\zeta_0,\tau)\cos\widetilde{\beta}(\zeta_0,\tau)}{\kappa(\zeta_0,\tau)\sqrt{1-\zeta_0^2}}d\zeta_0 + \frac{1}{\pi}\int\limits_{\zeta_0=1}^{b(\tau)}\frac{\gamma_s(\zeta_0,\tau)}{\kappa(\zeta_0,\tau)\sqrt{\zeta_0^2-1}}d\zeta_0 = 0. \tag{18}$$

The velocity continuity condition (18) is one of the three (two) relations needed to step-iterate the three (two) principal solution variables previously identified. The balance of the terms in (17) is then available for the analysis of the then non-singular $\gamma_c(\zeta, \tau)$ as:

$$\gamma_c(\zeta,\tau) = \frac{2}{\pi}\cos\widetilde{\beta}(\zeta,\tau)\left\{h_{c\tau}(\zeta,\tau)\sin\widetilde{\beta}(\zeta,\tau) - \zeta\kappa(\zeta,\tau)\sqrt{1-\zeta^2}\right.$$

$$\left. \times\left(2\int\limits_{\zeta_0=0}^{1}\frac{h_{c\tau}(\zeta_0,\tau)\cos\widetilde{\beta}(\zeta_0,\tau)}{\kappa(\zeta_0,\tau)\sqrt{1-\zeta_0^2}(\zeta_0^2-\zeta^2)}d\zeta_0 - \int\limits_{\zeta_0=1}^{b(\tau)}\frac{\gamma_s(\zeta_0,\tau)}{\kappa(\zeta_0,\tau)\sqrt{\zeta_0^2-1}(\zeta_0^2-\zeta^2)}d\zeta_0\right)\right\}. \tag{19}$$

Note from (19) that the cylinder drop velocity is not involved explicitly in the contour vortex strength.

2.2. CONTINUITY OF DISPLACEMENT

For the CUW flow regime it is necessary to require that the cylinder and free-surface contours at the jet head form a continuous contour, to first order. This is equivalent to continuity of mass, which to first order ignores the higher-order mass rate escaping through the jet. Similarly to the [3] development for the fixed-cylinder-contour geometry, the approach is to integrate the KBC, (9), across the small-time interval $\Delta\tau_i$ from $\tau_i - \Delta\tau_i$ to τ_i.

$$\Delta v_i^*(\xi) + \frac{1}{2}\Delta\gamma_{ci}^*(\xi)\sin\beta_i(\xi) = \Delta h_{ci}(\xi) - \Delta Y_{\mathrm{w}li}. \tag{20}$$

The subscript i in (20) denotes evaluation at the ith time, τ_i. The terms in (20) all represent changes in the respective displacement components across the time step. The independent variable ξ in (20) has replaced ζ to indicate non-dimensionalization on the jet-head offset z_{bi} rather than z_{ci}. The jet-head offset, z_{bi}, is the point of free-surface contour separation. The first term in (20) is again written in terms $\Delta\gamma_{ci}^*$ by the Biot-Savart law, but with the domain of ξ being (-1, 1):

$$\Delta v_i^*(\xi) = \frac{1}{2\pi}\int\limits_{\xi_0=-1}^{1}\frac{\Delta\gamma_{ci}^*(\xi_0)}{\xi_0-\xi}d\xi_0. \tag{21}$$

The solution to the Carleman equation (20) and (21) for $\Delta\gamma_{ci}^*$ proceeds just as did the solution to (9) and (10) for γ_c. Continuity of the displacement at $\xi = 1$ again requires that the terms singular as $1/\sqrt{1-\xi^2}$ be set collectively to zero. The displacement continuity condition, equivalent to (18) for velocity continuity, is therefore:

$$\Delta Y_{\mathrm{w}li} - \frac{2}{\pi}\int\limits_{\xi_0=0}^{1}\frac{\Delta h_{ci}(\xi_0)\cos\widetilde{\beta}_i(\xi_0)}{\kappa_i(\xi_0)\sqrt{1-\xi_0^2}}d\xi_0 = 0 \tag{22}$$

with

$$\kappa_i(\xi) \equiv \prod_{k=1}^{K}\left|\frac{\xi^2-\xi_{k+1}^{*2}}{\xi^2-\xi_k^{*2}}\right|^{\frac{\widetilde{\beta}_{ik}}{\pi}}. \tag{23}$$

The contour discretization represented by (23) is the same as at (14), and Figure 3, except for the non-dimensionalization on $z_b(\tau)$, *versus* $z_c(\tau)$.

Equation (22) provides the second relation among the three unknowns of the CUW problem.

2.3. CONTINUITY OF PRESSURE

The pressure continuity condition is unchanged from that developed in [3]. It is summarized here for completeness. The pressure coefficient in the $\zeta - \tau$ system of Figures 1 and 2 is written from the Bernoulli equations as:

$$C_p(\zeta, \tau) = V^2(\tau) - V_n^2(\zeta, \tau) - V_s^2(\zeta, \tau) + 2z_c(\tau) \left[\int\limits_{\zeta_0=\zeta}^{b(\tau)} V_s(\zeta_0, \tau)d\zeta_0 + \zeta V_s(\zeta, \tau) \right] +$$

$$+ 2z_c \left[\int\limits_{\zeta_0=\zeta}^{b(\tau)} V_{s\tau}(\zeta_0, \tau)d\zeta_0 + b_\tau(\tau)V_s(b, \tau) \right], \qquad 0 \le \zeta \le b(\tau). \tag{24}$$

C_p on the free-sheet segment $1 \le \zeta \le b(\tau)$ must be zero. Differentiation of (24) in ζ with C_p constant in ζ and τ gives the differential equation that the jet-head vortex strength $\gamma_s(\zeta, \tau) = -2V_s(\zeta, \tau)$ must satisfy:

$$(V_s - z_{c\tau}\zeta)V_{s\zeta} + z_c V_{s\tau} = 0, \qquad 1 \le \zeta \le b(\tau). \tag{25}$$

This is just the one-dimensional Euler equation on the relative stream $V_s - V_{z\tau}\zeta$. It states that the velocity of the fluid elements deposited onto the free-sheet at the jet head is constant in time thereafter at the separation value. This provides the procedure for developing the shed vortex sheets, with one element added to the sheet in each time step; [3] provides the details.

Equation (25) assures that the pressure is *constant* on the free sheet. The *zero value* of the constant is established by back substitution of (25) in (24):

$$0 = V^2(\tau) - V_n^2(\tau) - V_s^2(b, \tau) + 2(z_c b_\tau + z_{c\tau}b)V_s(b, \tau). \tag{26}$$

With $z_{b\tau}(\tau) \equiv z_c b_\tau + z_{c\tau}b$, (26) gives the formula:

$$z_{b\tau}(\tau) = \frac{V_s^2(b, \tau) + V_n^2(\tau) - V^2(\tau)}{2V_s(b, \tau)}. \tag{27}$$

On the free vortex sheet, to first order, $V_n = 0$ in (27) for the CUW flow, and $V_n = V$ for CW.

Equation (25) and formula (27) provide for pressure continuity on the free vortex sheet occupying $1 \le \zeta \le b(\tau)$.

3. Hydrodynamic analysis

The objective is to use the preceding results to compute the impact acceleration time history for a cylinder in free-drop, with specified contour geometry and geometric changes, $\beta_0(t)$ and $\delta(z, t)$, according to (1) and Figure 1.

A multi-layered, nested iteration of the nonlinear system of equations is required for advancing in time from the initial condition. Stable and robust numerical solution algorithms are essential, and are achieved here by reducing the mathematical solution as far as possible analytically before turning to the computer.

3.1. INITIALIZATION

The numerical procedure first reads the parameters for the ζ and τ discretizations, the fixed and time-variable contour geometry, $\beta_0(t)$ and $\delta(z, t)$, and the cylinder weight and drop height. The drop height, d, determines the initial impact velocity $V(0) = \sqrt{2gd}$ and the weight, W, along with the hydrodynamic forces, is needed for calculating the cylinder deceleration in any time interval.

For the work reported here, the space $0 \leq \zeta \leq 1$ is represented by 100 elements of lengths distributed to suit the physics, and 200 time steps are computed in $0 \leq \tau \leq 0.7$. For the contour discretization of Figure 3, the number of elements, K, is set as 25.

The initial condition is established from the wedge similarity solution at a small time interval $\Delta\tau_0$ after impact at $\tau = 0$; refer to [3]. The initial solution parameters of $V_s(1, \Delta\tau_0)$, $z_b(\Delta\tau_0)$ and $z_c(\Delta\tau_0)$, as well as the time derivatives $z_{b\tau}(\Delta\tau_0)$ and $z_{c\tau}(\Delta\tau_0)$, are established by the similarity solution. The initial similarity solution also provides the contour initial pressure distribution and hydrodynamic force, leading to a deceleration over the interval and a new, slightly reduced, impact velocity, $V(\Delta\tau_0) \equiv V(\tau_1) \equiv V_1$ to commence the non-similar integration in time.

3.2. SOLUTION ITERATION - CUW

The CUW phase occurs first in the flow development, and is the most important in the impact time history. At all time increments, including the first, the solution must be iterated using the *velocity continuity, displacement continuity*, and *pressure continuity* formulations of the preceding section.

At any time $\tau_i = \tau_{i-1} + \Delta\tau_i$, given the complete solution at τ_{i-1}, a new projected trial impact velocity V_i is first integrated over $\Delta\tau_i$ with V_{i-1} and $\dot{V}_{i-1}$ as:

$$V_i = V_{i-1} + \frac{1}{2}(\dot{V}_{i-1} + \dot{V}_i^I)\Delta\tau_i, \tag{28}$$

where $\dot{V}_i^I$ in (28) represents the Ith iterate in the outer-loop of the ith time step. The outer-loop convergence criteria is on $\dot{V}_i^I$.

The change in water-line is next calculated in the Ith loop iteration at time i, from (28):

$$\Delta Y_{\text{w}li} = \frac{1}{2}(V_i - V_{i-1})\Delta\tau_i. \tag{29}$$

3.2.1. *Jet head off-set Δz_{bi}, by displacement continuity*
From the waterline increment (29), the displacement continuity equation, (22), is iterated in a local inner loop. This local iteration is on Δz_{bi}, through the scaling variable $\xi = z/z_{bi}$ in (22). Taking $\Delta h_c(\xi) \cos \beta_i(\xi)$ as piecewise constant in Nz intervals over $0 \leq \xi \leq 1$, (22) becomes the following series:

$$\Delta Y_{\text{w}li} = \frac{1}{2\lambda_i} \sum_{j=1}^{Nz} \frac{\Delta h_{cij} \cos \widetilde{\beta}_{ij}}{\overline{\kappa}_{ij}} \left[\xi_n^{2\lambda_i} F(\lambda_i, \lambda_i, 1 + \lambda_i; \xi_n^2) \right]_{n=j}^{j+1}. \tag{30}$$

In (30), from Figure 3, $\lambda_j = \frac{1}{2} + \frac{\widetilde{\beta}_{iK}^*}{\pi}$ and F denotes the hypergeometric function of the first kind, [14]. The $\overline{\kappa}_{ij}$ function in (30) is from $\kappa_i(\xi)$ at (23). Equation (23) is first multiplied and divided by the factor $\left(\dfrac{1 - \xi^2}{\xi^2} \right)^{\frac{\widetilde{\beta}_{iK}^*}{\pi}}$. The divided factor remains with the balance of the integrand in (22) and is integrated piecewise in achieving the F-function in (30). This leaves the $\overline{\kappa}_i(\xi)$ function in (30):

$$\overline{\kappa}_i(\xi) = \left(\frac{1 - \xi^2}{\xi^2} \right)^{-\frac{\widetilde{\beta}_{iK}^*}{\pi}} \kappa_i(\xi). \tag{31}$$

Formula (31) is now written, using the explicit form of (23):

$$\overline{\kappa}_i(\xi) = \left(\frac{\xi_K^{*2} - \xi^2}{\xi^2} \right)^{-\frac{\widetilde{\beta}_{ik}^*}{\pi}} \prod_{k=1}^{K-1} \left| \frac{\xi_{k+1}^{*2} - \xi^2}{\xi_k^{*2} - \xi^2} \right|^{\frac{\widetilde{\beta}_{ik}^*}{\pi}}. \tag{32}$$

Formula (32) is a completely continuous function in $0 \leq \xi \leq 1$. It is slowly varying in ξ and has been extracted piecewise in discretizing the integral (22) to the form of (30). However, in order to avoid dealing numerically with the canceling singularities, the function (32) is fit at the following set: $\xi_1^* = 0$, $\xi_{K+1}^* = 1$ and at the Figure 3 element mid-points $\overline{\xi}_\ell^* = \frac{1}{2}(\xi_{\ell+1}^* + \xi_\ell^*)$, $\ell = 1, \ldots, K$. An interpolation then produces the Nz κ_{ij} set for use in (30):

$$\overline{\kappa}_{ij} = \left(\frac{\xi_K^{*2} - \overline{\xi}_j^2}{\overline{\xi}_j^2} \right)^{-\frac{\widetilde{\beta}_{iK}^*}{\pi}} \prod_{k=1}^{K-1} \left| \frac{\xi_{k+1}^{*2} - \overline{\xi}_j^2}{\xi_k^{*2} - \overline{\xi}_j^2} \right|^{\frac{\widetilde{\beta}_{iK}^*}{\pi}} \quad \overline{\xi}_j = \frac{1}{2}(\xi_{j+1} + \xi_j) \ \ j = 1, \ldots, Nz, \tag{33}$$

where Δz_{bi} in (30) is varied systematically until $\Delta Y_{\text{wl}i}$ by (30) is equal to the Ith iterate value at (29).

3.2.2. Jet velocity, V_{si1}, by pressure continuity

Pressure continuity is next used to calculate the fluid velocity entering the jet at the jet head, $V_{si}(b_i)$, from (25) and (27). Here an approximation has been made in the theory of [3]. In the original work the jet-head vortex strength is in a distribution of elements over the free sheet segment as prescribed by Euler's equation, (25) via the DBC. However, it was found, due to the extreme shortness of the free sheet segment in the CUW case, that numerical convergence was improved without loss of accuracy by representing the jet-head segment, 1 to $b(\tau)$, as one of uniform strength $\gamma_{si}(1)$, as in the similarity solution. From (1) and Figure 2:

$$V_{si}(bi) = V_{si}(1) \equiv V_{si1} = -\frac{1}{2}\gamma_{si1} \qquad \text{for the CUW case.} \tag{34}$$

Substitution in (27), with $V_{ni} = 0$ then gives:

$$V_{si1} = z_{bi\tau} + \sqrt{z_{bi\tau}^2 + V_i^2}, \tag{35}$$

where $z_{bi\tau} = \dfrac{\Delta z_{bi}}{\Delta \tau_i}$, with Δz_{bi} from the iteration at (36).

3.2.3. Zero pressure-point offset, z_{ci}, by velocity continuity

Finally, velocity continuity is applied to find z_{ci} in the current I^{th} iteration loop. Equation (18) is first rewritten for the Ith iterate of the ith time step as:

$$V_i - \frac{2}{\pi} \int\limits_{\zeta_0=0}^{1} \frac{h_{c\tau i}(\zeta_0) \cos \widetilde{\beta}_i(\zeta_0)}{\kappa_i(\zeta_0)\sqrt{1 - \zeta_0^2}} d\zeta_0 - \frac{2}{\pi} \int\limits_{\zeta_0=1}^{b_i} \frac{V_{si}(1)}{\kappa_i(\zeta_0)\sqrt{\zeta_0^2 - 1}} d\zeta_0 = 0. \tag{36}$$

The only unknown in (36) at this stage of the time i iteration is $b_i = z_{ci}/z_{bi}$, with z_{bi} known from the preceding displacement continuity calculation. The second term in (36) has the same general form as (30), and the third term, for the single free-sheet element of the CUW case, also integrates in terms of the hypergeometric function of the first kind. The result at (36) is:

$$V_i - \frac{1}{\pi \lambda_{ci}} \sum_{j=1}^{Nz} \frac{h_{c\tau ij} \cos \widetilde{\beta}_{ij}}{\overline{\kappa}_{cij}} \left[\zeta_m^{2\lambda_i} F(\lambda_{ci}, \lambda_{ci}, 1 + \lambda_{ci}; \zeta_m^2) \right]_{m=j}^{j+1} -$$

$$- \frac{1}{\pi \lambda_{si}} \frac{V_{si1}}{\overline{\kappa}_{si1}} (b_i^2 - 1)^{\lambda_{si}} F(\lambda_{si}, \lambda_{si}, 1 + \lambda_{si}; 1 - b_i^2) = 0. \tag{37}$$

In (37), in general, the subscript 'c' denotes cylinder material contour and 's' denotes free vortex sheet contour. Specifically:

$$\lambda_{ci} = \frac{1}{2} + \frac{\widetilde{\beta}_{iK}^*}{\pi}, \tag{38}$$

$$\lambda_{si} = \frac{1}{2} - \frac{\widetilde{\beta}_{iK}^*}{\pi}, \tag{39}$$

$$\overline{\kappa}_{cij} = \left(\frac{\zeta_K^{*2} - \overline{\zeta}_j^2}{\overline{\zeta}_j^2} \right)^{-\frac{\widetilde{\beta}_{iK}^*}{\pi}} \prod_{k=1}^{K-1} \left| \frac{\zeta_{k+1}^{*2} - \overline{\zeta}_j^2}{\zeta_k^{*2} - \overline{\zeta}_j^2} \right|^{\frac{\widetilde{\beta}_{ik}^*}{\pi}}, \quad \overline{\zeta}_j = \frac{1}{2}(\zeta_{j+1} + \zeta_j) \ j = 1, \dots, Nz, \tag{40}$$

$$\overline{\kappa}_{si1} = \left(\frac{\zeta_{i1}^2 - \zeta_K^{*2}}{\zeta_{i1}^2} \right)^{-\frac{\widetilde{\beta}_{iK}^*}{\pi}} \prod_{k=1}^{K-1} \left| \frac{\zeta_{i1}^2 - \zeta_{k+1}^{*2}}{\zeta_{i1}^2 - \zeta_k^{*2}} \right|^{\frac{\widetilde{\beta}_{ik}^*}{\pi}}, \quad \zeta_{i1} = \frac{1}{2}(1 + b_i). \tag{41}$$

Here, (38) and (40) are the same forms as for the displacement continuity condition, (30), but differ quantitatively due the scaling of z on z_{ci} rather than z_{bi} (Figure 3). (41) reflects the truncation of the free vortex sheet to the lead elements as discussed at (34). z_{ci} is determined through iteration of b_i, trancendentally, in satisfying (37).

3.2.4. *Contour vortex strength, $\gamma_{ci}(\zeta)$*

It is necessary at this stage to calculate the pressure and hydrodynamic force on the contour for evaluation of the acceleration $\dot{V}_i^{I+1}$ needed at the return to (28). The contour vortex strength needed for calculation of the cylinder contour pressure distribution is (19). From (19) at time i:

$$\gamma_{ci}(\zeta) = \frac{2}{\pi} \cos \widetilde{\beta}_i(\zeta) \left\{ h_{c\tau i}(\zeta) \sin \widetilde{\beta}_i(\zeta) - 2\zeta \kappa_i(\zeta) \sqrt{1 - \zeta^2} \right.$$

$$\times \left. \left(\int_{\zeta_0=0}^{1} \frac{h_{c\tau i}(\zeta_0) \cos \widetilde{\beta}_i(\zeta_0)}{\kappa_i(\zeta_0) \sqrt{1 - \zeta_0^2} (\zeta_0^2 - \zeta^2)} d\zeta_0 + V_{si1} \int_{\zeta_0=1}^{b_i} \frac{1}{\kappa_i(\zeta_0) \sqrt{\zeta_0^2 - 1} (\zeta_0^2 - \zeta^2)} d\zeta_0 \right) \right\} \tag{42}$$

$$0 \leq \zeta \leq 1$$

Separate this function into two:

$$\gamma_{ci}(\zeta) = \gamma_{cic}(\zeta) + \gamma_{cis}(\zeta). \tag{43}$$

Integration of the free sheet contribution, $\gamma_{cis}(\zeta)$, produces:

$$\gamma_{cis}(\zeta) = -\frac{2}{\pi} \frac{\overline{\kappa}_{ci}(\zeta) V_{si1} \cos \widetilde{\beta}_i(\zeta)}{\lambda_{si} \overline{\kappa}_{si1}} Q_{i1}(\zeta)^{\lambda_{si}} F[\lambda_{si}, \lambda_{si}, 1 + \lambda_{si}; Q_{i1}(\zeta)] \tag{44}$$

with: $Q_{i1}(\zeta) \equiv \dfrac{\zeta^2(b_i^2 - 1)}{b_i^2 - \zeta^2}$; λ_{si} and $\overline{\kappa}_{si1}$ in (44) are from (39) and (41); $\overline{\kappa}_{ci}(\zeta)$ is by (40) but at general ζ in $0 \leq \zeta \leq 1$. Formula (44) is singularity-free in $0 \leq \zeta \leq 1$ so that γ_{cis} is evaluated directly at the $Nz + 1$ element end points.

Reduction of the $\gamma_{cic}(\zeta)$ component of (42) proves to be a challenge because of the singular integrals. Write this component first as:

$$\gamma_{cic}(\zeta) = \frac{2}{\pi} \cos \widetilde{\beta}_i(\zeta) \left\{ h_{c\tau i}(\zeta) \sin \widetilde{\beta}_i(\zeta) - \right.$$

$$\left. -2\zeta \kappa_{ci}(\zeta)\sqrt{1 - \zeta^2} \sum_{j=1}^{Nz} \frac{h_{c\tau ij} \cos \widetilde{\beta}_{ij}}{\overline{\kappa}_{cij}} \int\limits_{\zeta_0 = \zeta_j}^{\zeta_{j+1}} \frac{\zeta_0^{\frac{2\widetilde{\beta}_{iK}^*}{\pi}}(1 - \zeta_0^2)^{-\frac{1}{2} - \frac{\widetilde{\beta}_{iK}^*}{\pi}}}{\zeta_0^2 - \zeta^2} d\zeta_0 \right\}. \tag{45}$$

Denote the integral in (45) as $\Delta I_{ij}(\zeta)$, and its integrand as $\mathrm{INT}_i(\zeta_0, \zeta)$. The ζ_j here are the end point offsets of the Nz elements in $0 \leq \zeta \leq 1$. I_{ij} has three different evaluations depending on the positions of the ζ_j, ζ_{j+1} integral limits relative to the singularity at ζ. These are denoted as follows:

For $\zeta > \zeta_{j+1}$:

$$I_{ij}^-(\zeta) \equiv \int\limits_{\zeta_0 = 0}^{\zeta_j} \mathrm{INT}_i(\zeta_0; \zeta) d\zeta_0 \quad \text{so that}: \quad \Delta I_{ij} = I_{ij+1}^- - I_{ij}^-, \tag{46}$$

For $\zeta < \zeta_j$:

$$I_{ij}^+(\zeta) \equiv \int\limits_{\zeta_0 = \zeta_j}^{1} \mathrm{INT}_i(\zeta_0; \zeta) d\zeta_0 \quad \text{so that}: \quad \Delta I_{ij} = I_{ij}^+ - I_{ij+1}^+, \tag{47}$$

For $\zeta_j < \zeta < \zeta_{j+1}$:

$$I_{ij}^0(\zeta) \equiv \int\limits_{\zeta_0 = 0}^{1} \mathrm{INT}_i(\zeta_0; \zeta) d\zeta_0 \quad \text{so that} \quad \Delta I_{ij} = I_{ij}^0 - I_{ij}^- - I_{ij+1}^+. \tag{48}$$

The integrals in (46) to (48) evaluate as follows:

$$I_{ij}^-(\zeta) = -\frac{1}{2\lambda_i^- \zeta^2} \left(\frac{\zeta_j^2}{1 - \zeta_j^2} \right)^{\lambda_i^-} F\left[\lambda_i^-, 1, 1 + \lambda_i^-; \left(\frac{\zeta_j}{\zeta} \right)^2 \left(\frac{1 - \zeta^2}{1 - \zeta_j^2} \right) \right] \tag{49}$$

with $\lambda_i^- \equiv \dfrac{1}{2} + \dfrac{\widetilde{\beta}_{iK}^*}{\pi}$,

$$I_{ij}^+(\zeta) = \frac{1}{2\lambda_i^+(1 - \zeta^2)} \left(\frac{1 - \zeta_j^2}{\zeta_j} \right)^{\lambda_i^+} F\left[\lambda_i^+, 1, 1 + \lambda_i^+; \left(\frac{\zeta}{\zeta_j} \right)^2 \left(\frac{1 - \zeta_j^2}{1 - \zeta^2} \right) \right] \tag{50}$$

with $\lambda_i^+ \equiv \dfrac{1}{2} - \dfrac{\widetilde{\beta}_{iK}^*}{\pi}$,

$$I_{ij}^0(\zeta) = \frac{\pi \, \tan \widetilde{\beta}_{iK}^*}{2\zeta \sqrt{1-\zeta^2}} \left(\frac{\zeta^2}{1-\zeta^2} \right)^{\frac{\widetilde{\beta}_{iK}^*}{\pi}}. \tag{51}$$

Formula (45) is evaluated at the centers of the Nz elements in $0 \le \zeta \le 1$ as:

$$\gamma_{cic}(\overline{\zeta}_\ell) = \frac{2}{\pi} \cos \widetilde{\beta}_i(\overline{\zeta}_\ell) \left\{ h_{c\tau i}(\overline{\zeta}_\ell) \sin \widetilde{\beta}_i(\overline{\zeta}_\ell) - 2\overline{\zeta}_\ell \kappa_{ci}(\overline{\zeta}_\ell) \sqrt{1-\overline{\zeta}_\ell^2} \sum_{j=1}^{Nz} \frac{h_{c\tau ij} \cos \widetilde{\beta}_{ij}}{\overline{\kappa}_{cij}} \Delta I_{ij}(\overline{\zeta}_\ell) \right. ,$$

$$\text{where}: \overline{\zeta}_\ell = \tfrac{1}{2}(\zeta_\ell + \zeta_{\ell+1}) \quad \ell = 1, \dots, Nz. \tag{52}$$

The values at the contour element end-point are then interpolated from (52).

3.3. SOLUTION ITERATION - CW

The chine-wetted (CW) phase of the impact commences at the time that the zero pressure offset, $z_c(\tau)$, reaches the chine, $Z_{ch}(\tau)$. Refer to Figure 1. After this time $z_c(\tau)$ is constrained to the known $Z_{ch}(\tau)$, but $z_b(\tau)$ continues its traverse on out across the free-surface. The hydrodynamic theory covering the CW case and the hydrodynamic analysis is the same as developed in the preceding subsection for the CUW flow, except in two respects. (1) There is one less parameter unknown (z_c) and one less solution condition: displacement continuity; (2) With continuing outward progression of the jet head relative to the chine, the vortex sheet $z_c(\tau)$-to-$z_b(\tau)$ cannot be represented by a single element in the pressure and velocity continuity conditions.

The two principal parameter unknowns here are the jet-head velocity $z_{bi\tau}$ and the chine separation velocity V_{si1}.

Define the number of time steps to chine wetting i_{cw} and the time as $\tau_{icw} = \tau_{i-1} + \Delta\tau_{icw}$. $\Delta\tau_{icw}$ is interpolated from the initially set value at this i, along with the other solution variables involving time integration. The iteration therefore resumes at the start of a new outer loop at (28) at $i = i_{cw} + 1$.

3.3.1. *Pressure continuity*
The jet-head velocity at time i is (27):

$$z_{bi\tau} = \frac{V_{si}^2(b_i) + V_{ni}^2 - V_i^2}{2V_{si}(b_i)}. \tag{53}$$

In the downward-moving coordinate system the velocity normal to the free surface is V_i to first order. Formula (53) is therefore reduced to:

$$z_{bi\tau} = \frac{V_{si}(b_i)}{2}. \tag{54}$$

The implementation here is exactly as covered in [3]. In the interest of summary, the difficulty here is that the velocity $V_{si}(b_i)$ in (54) is now the jet velocity at the jet-head, $z_{bi} = z_{ci}b_i$, and not the jet velocity V_{si1} at jet separation, z_{ci}.

The free-vortex sheet between z_{ci} and z_{bi} is composed of vortex elements, with one new element added at z_{ci} in each time step. The balance of the elements in the sheet redistribute as required by (25) to-satisfy the Eulers equation of zero particle acceleration. But the new element added at z_{ci} has unknown velocity V_{si1} as well as unknown length δb_{i1}. The relative lengths of the sheet elements are denoted as δb_{ij}, with end points at ζ_{ij}, and the element

velocities are denoted as V_{sij}; $j = 1, n_i$. n_i is the number of elements in the sheet at time i, which is equal to the number of time steps beyond chine-wetting. Refer to Figures 7 and 8 of [3]. Here b_i is related to the δb_{ij} and ζ_{ij} by:

$$\zeta_{ij} = 1 + \sum_{k=1}^{j} \delta b_{ij} \equiv \zeta_{ij-1} + \delta b_{ij} \quad j = 1, \ldots, n_i; \quad b_i = \zeta_{in_i} \tag{55}$$

and

$$\delta b_{ij} = \frac{\delta z_{bn_i-j+1}}{z_{ci}} \text{with} \quad \delta z_{bi} = (z_{bi\tau} - z_{ci\tau})\Delta \tau_i. \tag{56}$$

With all V_{sij} and δb_{ij}, from $j = 2, \ldots, n_i$ known from previous time steps, the selection of a trial V_{si1} determines an iterate of the unknown δb_{i1}, and therefore $z_{bi\tau}$ and z_{bi}, by way of (54), (55), and (56). An essential difference numerically relative to the CUW case is that V_{si1} and δb_{i1} are in coupled, rather than uncoupled, iteration loops within the outer loop on V_i.

3.3.2. *Velocity continuity*
V_{si1}, for the δb_{i1} iterate determined as above, is from velocity continuity. The discretization of (18) for the CW case now includes the full free-sheet induction with n_i elements. Comparing to (37):

$$V_i - \frac{1}{2\lambda_{ci}} \sum_{j=1}^{Nz} \frac{h_{c\tau ij} \cos \widetilde{\beta}_{ij}}{\overline{\kappa}_{cij}} \left[\zeta_{im}^{2\lambda_i} F(\lambda_{ci}, \lambda_{ci}, 1 + \lambda_{ci}; \zeta_{im}^2) \right]_{m=j}^{j+1} - $$
$$- \frac{1}{\lambda_{si}} \sum_{j=1}^{n_i} \frac{V_{sij}}{\overline{\kappa}_{sij}} \left[(\zeta_{im}^2 - 1)^{\lambda_{si}} F(\lambda_{si}, \lambda_{si}, 1 + \lambda_{si}; 1 - \zeta_{im}^2) \right]_{m=j-1}^{j} = 0. \tag{57}$$

The λ's and $\overline{\kappa}$'s in (57) are the same as (38) to (41) for CUW, except $\overline{\kappa}_{sij}$ is here generalized for $j = 1, \ldots, n_i$ sheet elements.

3.3.3. *Contour vortex strength, $\gamma_{ci}(\zeta)$*
The contour vortex strength again differs from the CUW case only as to the free sheet vortex element number. For $\gamma_{ci}(\zeta)$ written again as (43),

$$\gamma_{ci}(\zeta) = \gamma_{cic}(\zeta) + \gamma_{cis}(\zeta) \tag{43}$$

the expansion is in $\gamma_{cis}(\zeta)$ only:

$$\gamma_{cis}(\zeta) = -\frac{2}{\pi} \frac{\overline{\kappa}_{ci}(\zeta) \cos \widetilde{\beta}_i(\zeta)}{\lambda_{si}} \sum_{j=1}^{n_i} \frac{V_{sij}}{\overline{\kappa}_{sij}} \left(Q_{im}(\zeta)^{\lambda_{si}} F[\lambda_{si}, \lambda_{si}, 1 + \lambda_{si}; Q_{im}(\zeta)] \right)_{m=j}^{j+1} \tag{58}$$

with $Q_{ij}(\zeta)$ in (58) generalized from (44) by replacing b_i by ζ_{ij}.

3.4. PRESSURE AND SECTIONAL FORCE COMPUTATION

Substitution of (25) and (26) in (24) gives the pressure on the cylinder contour, for either the CUW or CW cases, as:

$$C_{pi}(\zeta) = \frac{1}{4} \left[\gamma_{ci}^2(1) - \gamma_{ci}^2(\zeta) \right] - z_{ci\tau} \left[\int_{\zeta_0=\zeta}^{1} \gamma_{ci}(\zeta_0) d\zeta_0 + \zeta \gamma_{ci}(\zeta) - \gamma_{ci}(1) \right] - z_{ci} \int_{\zeta_0=\zeta}^{1} \gamma_{ci\tau}(\zeta_0) d\zeta_0. \tag{59}$$

The second and third groups of terms in (59) are the time rate-of-change of velocity potential on the contour. The $\zeta_{ci\tau}$ derivative in the last integral is computed as a backward difference across the time step.

In passing, it is here that coupling of the pressure distribution with the structural model for calculating the deflection distribution to start the next iterate at time i is effected in the complete analysis Vorus and Royce [9].

The hydrodynamic force per unit length of the cylinder is, from (59):

$$C_{fi} \equiv \frac{f_i}{\frac{1}{2}\rho V_0^2 Z_{ch0}} = 2z_{ci} \int\limits_{\zeta=0}^{1} C_{pi}(\zeta)\mathrm{d}\zeta. \tag{60}$$

3.5. IMPACT ACCELERATION COMPUTATION

This concludes the calculations of the Ith loop iteration at time i. The cylinder impact acceleration to initiate the $I + 1$ iteration loop of the ith time step at (28) is:

$$\dot{V}_i^{I+1} = \frac{C_{fi} - C_w}{C_m}, \tag{61}$$

where C_w is the cylinder weight coefficient,

$$C_w = \frac{w}{\frac{1}{2}\rho g V_0^2 Z_{ch0}}, \tag{62}$$

and w is the cylinder weight per unit length. C_w also equals the mass coefficient,

$$C_m = C_w = \frac{m}{\frac{1}{2}\rho V_0^2 z_{ch0}}. \tag{63}$$

The looping between (28) and (61) continues in the ith time step until the change from $\dot{V}_i^I$ to $\dot{V}_i^{I+1}$ is sufficiently small. Time is then incremented from i to $i + 1$ and the iteration restarted, and so on, until the solution has been computed for the total time specified.

4. Computations

4.1. INPUT DATA

As explained in the introduction, the cylinder deflection data, $\beta_0(t)$ and $\delta(z, t)$, Figure 1, that has been selected for demonstration of the preceding analysis formulation is essentially that from the cylinder drop test simulations reported in [9]. Figure 4 is a plot of the nose-tail line angle $\Delta\beta_0(\tau) = \beta_0(\tau) - \beta_0(0)$, degrees, versus $\tau = V_0 t/Z_{ch}$, over the $0 \leq \tau \leq 0.7$ duration of the calculation.

Figure 4 shows only the change in deadrise angle associated with the cylinder compliance. This must be added to the 20 deg $\beta_0(0)$ angle of the unflexed cylinder in constructing equation (2); refer to Figure 7. In the time non-dimensionalization, Z_{ch} is the chine offset, which is fixed in time for these calculations: $Z_{ch}(t) = Z_{ch}(0) = Z_{ch}$. V_0 is the initial impact velocity, as addressed at Figure 2.
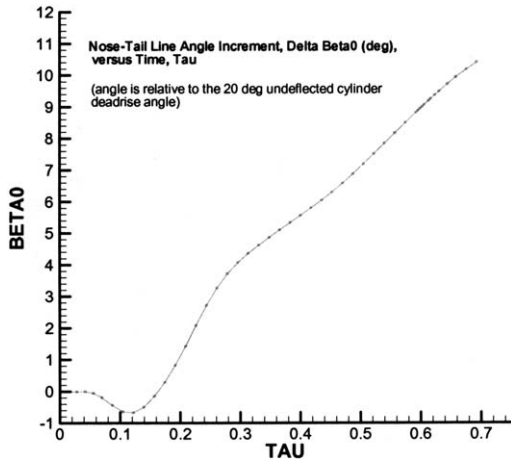
Figure 4. Nose-tail line angle variation with time, $\beta_0(\tau)$, for impact acceleration computations.
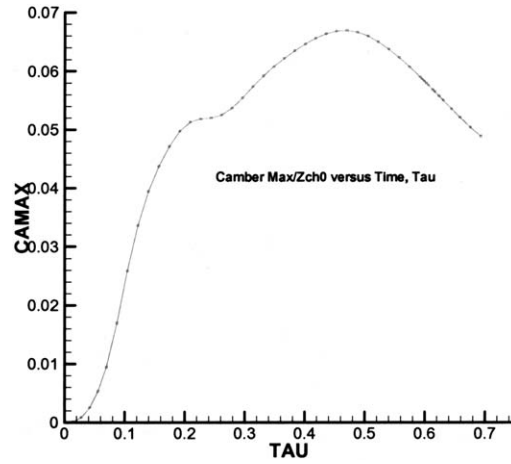
Figure 5. Nose-tail line maximum camber variation with time, $\delta_{\max}(z, \tau)$, for impact acceleration computations.
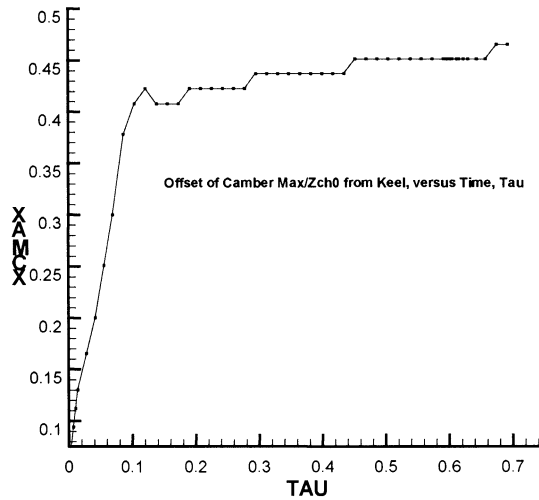

Figure 6. Nose-tail line maximum camber offset variation with time for impact acceleration computations.

Figure 5 is the variation with τ of the camber maximum, $\delta_{\max}(z, \tau)$, non-dimensioned on Z_{ch}. Camber is defined, in the sense of a hydrofoil section, as the offset normal to the inclining $\beta_0(t)$-nose-tail line at any time. Figure 6 is the offset of the camber maximum transversely from the keel, also dimensionless on Z_{ch}.

The camber is approximately cubic in z, zero at $z/Z_{\mathrm{ch}} = 0$ and 1, by definition, with the maximum shifting outward in time, as indicated by Figure 6.

The composite deflection assembled by (1) from the β_0 and δ data of Figures 4, 5, and 6 is shown on Figure 7. Figures 7a and 7b are the body-plans, to scale, of the rigid and flexing cylinder, as it falls through the free surface at $y = 0$. On Figure 7, $\zeta = 1$ is the chine half-beam. The figure is plotted for the deflection distribution over the half-beam for 51 values of time in $0 \leq \tau \leq 0.7$. The sectional lines on Figure 7 correspond to the depth of the cylinder,
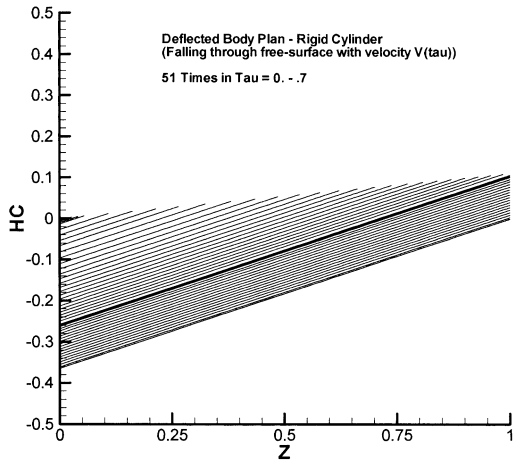
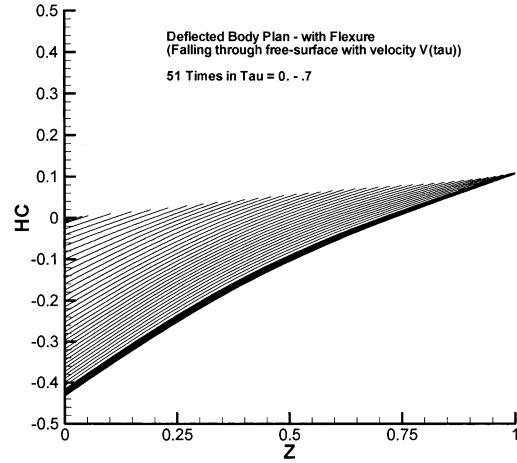*Figure 7a.* Body plan for rigid cylinder falling with velocity $V(\tau)$ through free-surface.

Figure 7b. Body plan for flexing cylinder falling with velocity $V(\tau)$ through free-surface.

$y_c(\zeta, \tau)$, (1), at the 51 times τ from initial entry, the upper line set, at $\tau = 0$, to the deepest at the final time $\tau = 0.7$. The extents of the contour lines are to the zero pressure point, which is $z_c(\tau)$ for $\tau < \tau_{\mathrm{cw}}$ and Z_{ch} after chine wetting. The concentrations of contour lines on both Figures 7a and 7b correspond to the reduction in time increment in the immediate vicinity of chine wetting.

From a comparison of the data of Figures 7a and 7b, the relative maximum where flexural deflection space occurs at the chine with a value less than 10% of the cylinder chine beam.

4.2. HYDRODYNAMIC CALCULATIONS

4.2.1. *Impact acceleration, velocity, and pressure distributions*

The predicted impact acceleration and cylinder downward velocity versus time for both the rigid and the deflecting cylinder is shown on Figure 8.

The velocities in Figure 8 are dimensionless on V_0 and the accelerations as VDOT $\equiv$ $\dfrac{\dot{V}(t)Z_{\mathrm{ch}}}{V_0^2}$. With dimensionless gravity defined as $G \equiv \dfrac{gZ_{\mathrm{ch}}}{V_0^2}$, the impact acceleration in g's is VDOT/G.

For the case developed here, from [9], the cylinder half-beam, Z_{ch}, is 1 ft = 0·305 m. With a drop height $d = 4$ ft (1·22 m), the initial impact velocity is:

$$V_0 = \sqrt{2gd} = 4.89 \text{ m/sec}.$$

This gives a total time for the computations as $t_{\max} = \tau_{\max} Z_{\mathrm{ch}}/V_0 = 0.0436$ sec. The cylinder dimensionless weight, (63), is 0·17 and the dimensionless gravity $G = 0.125$. With this G, the maximum impact acceleration of Figure 8, corresponding to the rigid cylinder, is therefore approximately $2.7/0.125 = 21.6$ g's. The maximum acceleration of the cylinder with flexure, from Figure 8, is approximately VDOT $= 1.4$, implying a maximum acceleration in g's of $1.4/0.125 = 11.2$. The reduction in impact acceleration with the particular hull deflection characteristic specified is implied by Figure 8 to be essentially 50%.
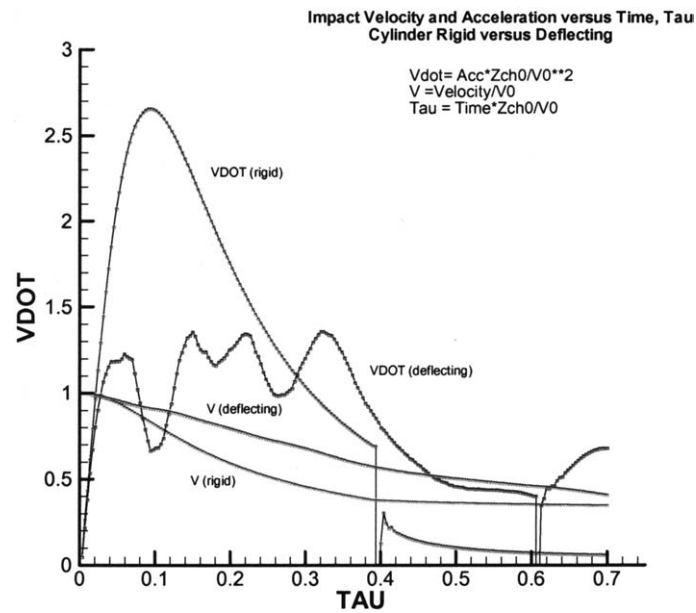
Figure 8 Impact velocity and acceleration versus time, predicted for the rigid and deflecting cases.

This result is consistent with the calculated performance of the LocalFlex system reported in [9], only better, by around 10%. The calculated distribution of acceleration now also matches better with the experimental data presented in that reference as to the level and phase of the flexural oscillations that occur in time. The improvement is due to elimination of an inconsistency in the predictive code, which is also reflected in the theoretical development presented here. Although the LocalFlex air bag model incorporated in the original analysis has not changed, this is not particularly relevant here, as the source of the deflection input of Figures 4–7 is not a focus of this work. The focus is only to demonstrate the level of impact reduction possible with surface flexural dynamics, however such might be produced.

With regard to the Figure 8 accelerations, the reason for the single narrow peak in the rigid cylinder characteristic is clearly the superposition of the two opposite effects influencing the impact force; these are expanding cylinder breadth and decreasing downward velocity with time. Early in the slam the increasing breadth, occurring at high velocity initially, outweighs the rate of velocity reduction, but the roles reverse with time, leaving a clean impact force maximum, and therefore the acceleration peak.

The times of chine wetting for the two cases are also evident on Figure 8 as the discontinuities appearing in the acceleration curves. This behavior occurs in the calculation due to the negative infinite rate-of-change of $z_c(t)$ with time at the abrupt encounter with the chine. Although second-order flow effects do eliminate this singularity in the real-flow physics, its appearance in the analysis is believed to be inconsequential to predictions of interest.

Note also from Figure 8 that even though the impact velocity for the deflecting cylinder, with the lower impact acceleration, remains at a higher level resulting in more rapid penetration depth, the time to chine-wetting is increased. This may appear initially to be a contradiction; the explanation is that the chine is rising with time as the plating deflects upward, as shown by a comparison of Figures 7a and 7b.
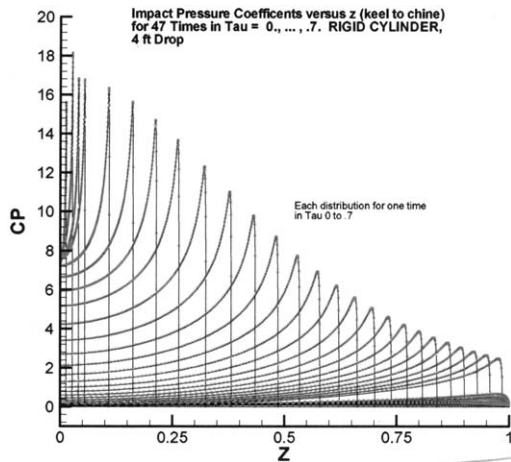
Figure 9. Pressure distributions in z for rigid cylinder for values of time, from Equation (59).
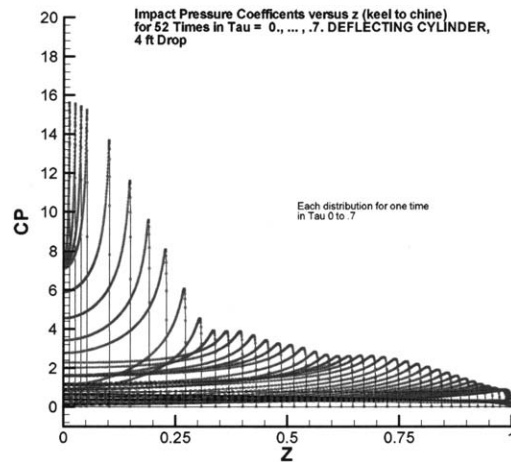

Figure 10. Pressure distributions in z for compliant cylinder for values of time, from Equation (59).

The pressure distributions versus z for values of time are plotted on Figures 9 and 10 for the rigid and compliant cases, respectively. The pressure falls rapidly enough in the compliant case to significantly limit the expanding breadth effect in amplifying the impact force with time progression.

In Figure 10, the oscillations which appear in the accelerations of Figure 8 are also seen in the compliant-cylinder pressure distribution at the same times in the slam, but not as pronounced due to the relative scale. These relatively low-level oscillations occur in the dynamics of the plating flexure exhibited in Figure 7b (as better seen in Figure 11 to follow).

4.2.2. *Deflection and contour wetting*
The deflection contours, Figure 7, are revealing with regard to the detailed physics of the impact processes demonstrated on Figure 8. A twice-vertical scale version of the flexural part of Figure 7b, relative to the cylinder, is added as Figure 11. This is for elucidating the driving hydrodynamics of Figure 8.

The Figure 11 curves represent the full deflection of the contour out to the chine at all 51 times; Figure 7 plots the deflections only out to $z_c(\tau)$. The faint (overlaid) symbols added to the Figure 7b deflection curves in Figure 11 indicate the position of the zero-pressure offset, $z_c(\tau)$, at the respective times. This corresponds to the loaded length of the section at each time, and equal to the lengths of the pressure curves on Figure 10.

The impact acceleration reduction achieved by the upward plate deflection can be viewed as producing a negative added mass. This superimposes with the positive added mass due to the generally downward velocity of the cylinder. This is a correct view, but incomplete. 'Arching' of the plate must be minimized. Arching produces a positive convective pressure that tends to nullify the favorable negative temporal component accompanying the relative upward movement. This pressure amplifying effect of arching is, for example, much as in a 'flare-slam' of a displacement vessels with concave side-shell camber in the bow region.

Ando, [15], concluded that plating flexibility could not be used as a device for reducing impact in V-bottom boats because the adverse effects of the 'arching' more than offset the
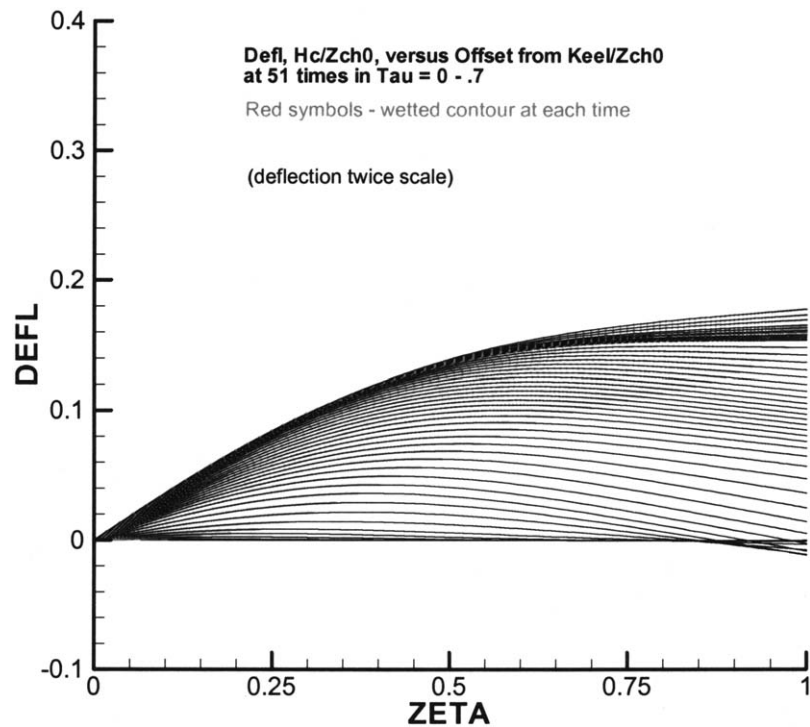
Figure 11. Composite Deflection, $\Delta h_c(z/Z_{ch}, \tau)$ by equation (2) (twice vertical scale).

beneficial effects of the plate flexibility. But that work not only ignored the plating dynamics that must be exploited, but assumed the plate to be pinned at both the keel and the chine ends.

The key to the effectiveness of the Figure 11 deflection characteristic is the rapid upward movement of the plate tip at the chine. This is in the sense of 'cracking a whip'. A desirable hydrodynamic objective is achieved, which is clearly exhibited in Figure 11: The goal with compliance of this type is to have the end of the pressure curve always moving upward in time. As noted from Figures 9 and 10, the CUW pressure distribution peaks very near the end of the pressure curve at any time. If the end of the pressure curve is always rising, the increasing wetting figuratively tends to roll the pressure peak outward and off the chine. The achievement is reduction in the slam intensity, as exhibited on Figure 8.

5. Conclusion

This paper has dealt with only part of the analysis capability needed for full study and development of compliant-surface concepts for wave-impact shock reduction of high-speed planing craft. It has presented a robust and theoretically consistent theory and analysis of hydrodynamics of hull-surface pressure distributions and resulting impact forces and accelerations for specified spatio-temporal hull-surface deflection distributions. This analysis must be mated with mechanisms for controlling the compliant distributions to maximize the shock reduction results sought. The LocalFlex system reported by [9] is a first effort in this direction. The hull compliance characteristics of the development of [9], demonstrated here, appear to be of the type to be potentially attractive for practical applications in high-speed craft. The 'LocalFlex' compliance appears to have a potential effectiveness level of at least 50% reduction of wave

impact acceleration, and it should not require an unreasonable space envelope within the boat. The vertical depth requirement is predicted to be no greater than around 10% of the craft beam. And since the slam, at least as to origin, is believed to be typically centered just forward of mid-boat, the shock reduction installation might be limited to a relatively small fraction of the boat length in that region.

The major difficulty in developing an operational system of this type appears to be its actuation. For the boat sizes and speeds for which this type of technology is so badly needed, the typical operating seaway suggest slams occurring every one to two seconds. Cycling of the system from slam deflection to redeployment to re-actuation, etc., would require achievement on what would appear to be a severely short time scale relative to the geometric and inertial scales imposed.

While some work has been done by this author on practical implementation, further effort, and effort by others, is needed. The hydrodynamic theory presented here is offered as a basis for continuing work. It is believed to be capable of relatively reliable analysis of concept trade-offs, as is essential, in general, for the successful development of new engineering design. This is here, specifically, to allow high speed boats to run at higher speed in rough sea conditions.

Acknowledgements

Appendix. Kinematic boundary condition for rigid cylinder impact integral equation solution

A1. GENERAL SOLUTION

Application of the kinematic boundary condition of zero normal velocity on the bottom of the rigid, relatively flat, cylinder, impacting the surface with velocity $V(t)$, produces a linear one-dimensional integral equation to be inverted for the wetted contour vortex strength $\gamma_c(\zeta, \tau)$; refer to text Equation (11):

$$\frac{1}{2}\gamma_c(\zeta, \tau)\sin\beta(\zeta, \tau) + \frac{1}{2\pi}\int_{\zeta_0=-1}^{1}\frac{\gamma_c(\zeta_0, \tau)}{\zeta_0 - \zeta}d\zeta_0 = -V(\tau) - \frac{1}{\pi}\int_{\zeta_0=1}^{b(\tau)}\frac{\gamma_s(\zeta_0, \tau)}{\zeta_0^2 - \zeta^2}d\zeta_0 \quad 0 \leq \zeta \leq 1. \tag{A1}$$

From Tricomi, [16, Section 4.4] or Muskhelishvili, [13, Section 81], (A1) is a singular integral equation of the Carleman type, of the general form:

$$a(\zeta)\gamma_c(\zeta) - \frac{1}{\lambda}\int_{\zeta_0=-1}^{1}\frac{\gamma_c(\zeta_0)}{\zeta_0 - \zeta}d\zeta_0 = f(\zeta), \qquad -1 \leq \zeta \leq 1. \tag{A2}$$

All singular integrals appearing here and in the following are to be interpreted as principal value integrals.

Comparing (A1) and (A2): $a(\zeta) = \mp\sin\beta(\zeta)$ on the complete interval $-1 \leq \zeta \leq 1$. Also,

$$\lambda = -\frac{1}{\pi} \quad \text{and} \quad f(\zeta) \equiv -2V - \frac{2}{\pi} \int\limits_{\zeta_0=1}^{b} \frac{\gamma_s(\zeta_0)\zeta_0}{\zeta_0^2 - \zeta^2} d\zeta_0. \tag{A3}$$

Time, τ, acts as a parameter in (A2) and is not explicitly shown for convenience of notation.

Following [13, pp. 235–238], (A2) represents a non-homogeneous Hilbert problem for open contours, or 'arcs'. The two arcs in this case are the two segments $-1 < \zeta < 0$ and $0 < \zeta < 1$ on the ζ-axis; $\gamma_c(\zeta)$ is holomorphic on each of these two arcs. The solution of (A2) is:

$$\gamma_c(\zeta) = \frac{a(\zeta)f(\zeta)}{a^2(\zeta) + \pi^2\lambda^2} + \frac{\lambda\chi(\zeta)}{\sqrt{a^2(\zeta) + \pi^2\lambda^2}} \int\limits_{\zeta_0=-1}^{1} \frac{f(\zeta_0)d\zeta_0}{\sqrt{a^2(\zeta_0) + \pi^2\lambda^2}\chi(\zeta_0)(\zeta_0 - \zeta)}. \tag{A4}$$

Define:

$$\widetilde{\beta}(\zeta) = \tan^{-1}[\sin \beta(\zeta)]. \tag{A5}$$

(A5) can then be written:

$$\gamma_c(\zeta) = \sin \widetilde{\beta}(\zeta) \cos \widetilde{\beta}(\zeta) f(\zeta) - \frac{\cos \widetilde{\beta}(\zeta)}{\pi} \chi(\zeta) \int\limits_{\zeta_0=-1}^{1} \frac{\cos \beta(\zeta_0) f(\zeta_0)}{\chi(\zeta_0)(\zeta_0 - \zeta)} d\zeta_0. \tag{A6}$$

From [13], the function $\chi(\zeta)$ in (A4) and (A6) is, in general,

$$\chi(\zeta) = P(\zeta)e^{\tau(\zeta)} \tag{A7}$$

with,

$$P(\zeta) = \prod_{m=1}^{2p}(\zeta - c_m)^{\lambda_m} \tag{A8}$$

and,

$$\tau(\zeta) = \frac{1}{\pi}\sum_{k=1}^{p}\int\limits_{L_k}\frac{\theta(t)dt}{t - \zeta} \tag{A9}$$

with,

$$\theta(\zeta) = \tan^{-1}\frac{\lambda\pi}{a(\zeta)} \qquad 0 \leq \theta \leq 2\pi, \tag{A10}$$

In (A8) and (A9), p is the number of arcs, whose end points have coordinates c_m. The λ_m are integers selected according to the character of the function at the end points of the respective arcs L_k.

For this specific problem: $p = 2$ and the four c_m are $-1, 0; 0, 1$. Therefore, (A8) is:

$$P(\zeta) = (1 + \zeta)^{\lambda_1}\zeta^{(\lambda_2+\lambda_3)}(1 - \zeta)^{\lambda_4}. \tag{A11}$$

But by the criterion of Muskhelishvili, [13, pp. 235–288], $\zeta = \pm 1, \pm 0$ qualify as 'non-special' ends, so that the choice of λ_k is to suit the choice of boundedness of $\gamma_c(\zeta)$ at the respective end points, $\zeta \to c_m$.

Turning to (A9) and (A10):

$$\tau(\zeta) = \frac{1}{\pi} \int\limits_{t=-1}^{0} \frac{\theta^-(t)}{t-\zeta} dt + \frac{1}{\pi} \int\limits_{t=0}^{1} \frac{\theta^+(t)}{t-\zeta} dt \tag{A12}$$

From (A5) and (A10), with $a(\zeta) = \mp \sin \beta(\zeta)$,

$$\theta^\pm(\zeta) = -\frac{\pi}{2} \mp \widetilde{\beta}(\zeta). \tag{A13}$$

Substitute (A13) in (A12) and integrate:

$$\tau(\zeta) = \log \sqrt{\frac{1+\zeta}{1-\zeta}} + \frac{1}{\pi} \int\limits_{t=0}^{1} \widetilde{\beta}(t) \left(\frac{1}{t-\zeta} + \frac{1}{t+\zeta} \right) dt. \tag{A14}$$

A2. SPECIFIC SOLUTION

At this point it is necessary to specify the form of $\widetilde{\beta}(\zeta)$ in order to continue the analytical development beyond (A14). Referring to Figure 3 of the text, represent the cylinder contour in $0 \le \zeta \le 1$ as piecewise linear with K elements, so that $\beta(\zeta)$, and hence $\widetilde{\beta}(\zeta)$ by (A5), are piecewise constant. The piecewise constant values of $\beta(\zeta)$ are denoted as $\beta_k^*, k = 1, K$, by Figure 3.

The Figure 3 discretization reduces (A14) to:

$$\tau(\zeta) = \log \sqrt{\frac{1+\zeta}{1-\zeta}} + \frac{1}{\pi} \sum_{k=1}^{K} \widetilde{\beta}_k^* \log \left| \frac{\zeta^2 - \zeta_{k+1}^{*2}}{\zeta^2 - \zeta_k^{*2}} \right| \tag{A15}$$

Combining further in (A15),

$$\tau(\zeta) = \log \left[\sqrt{\frac{1+\zeta}{1-\zeta}} \prod_{k=1}^{K} \left| \frac{\zeta^2 - \zeta_{k+1}^{*2}}{\zeta^2 - \zeta_k^{*2}} \right|^{\frac{\widetilde{\beta}_k^*}{\pi}} \right] \tag{A16}$$

Now substitute (A11) and (A16) back into (A7) to obtain the $\chi(\zeta)$ function in the solution (A6) as:

$$\chi(\zeta) = (1+\zeta)^{\lambda_1} \zeta^{(\lambda_2+\lambda_3)} (1-\zeta)^{\lambda_4} \sqrt{\frac{1+\zeta}{1-\zeta}} \prod_{k=1}^{K} \left| \frac{\zeta^2 - \zeta_{k+1}^{*2}}{\zeta^2 - \zeta_k^{*2}} \right|^{\frac{\widetilde{\beta}_k^*}{\pi}} \tag{A17}$$

At this point the λ_m in (A17) can be specified. In order that the solution exhibit the necessary symmetry, the unique choice is $\lambda_1 = -1, \lambda_2 = \lambda_3 = \lambda_4 = 0$. This gives, from (A17):

$$\chi(\zeta) = \frac{1}{\sqrt{1-\zeta^2}} \prod_{k=1}^{K} \left| \frac{\zeta^2 - \zeta_{k+1}^{*2}}{\zeta^2 - \zeta_k^{*2}} \right|^{\frac{\widetilde{\beta}_k^*}{\pi}}. \tag{A18}$$

With this choice of the λ_m the square-root singularity is placed at $\zeta \pm 1$; this will ultimately be removed by the velocity continuity (Kutta) condition imposed on the system solution. It is to be understood from the principal value integral at (A12) that $\zeta \ne \zeta_k^*$ in (A18) so that $\chi(\zeta)$ is continuous in $0 < |\zeta| < 1$.

Write (A18) for later use as

$$\chi(\zeta) \equiv \frac{\kappa(\zeta)}{\sqrt{1-\zeta^2}} \tag{A19}$$

with

$$\kappa(\zeta) = \prod_{k=1}^{K} \left| \frac{\zeta^2 - \zeta_{k+1}^{*2}}{\zeta^2 - \zeta_k^{*2}} \right|^{\frac{\widetilde{\beta}_k^*}{\pi}}. \tag{A20}$$

It is now necessary to substitute the specific form of $f(\zeta)$, (A3), into the solution (A6), and to perform the indicated operations. An intermediate result that follows is:

$$\gamma_c(\zeta) = 2 \cos \widetilde{\beta}(\zeta) \left\{ \left[\frac{1}{\pi} \chi(\zeta)\Lambda(\zeta) - \sin \widetilde{\beta}(\zeta) \right] \left[V + \frac{1}{\pi} \int_{t=1}^{b} \frac{\gamma_s(t)dt}{t^2 - \zeta^2} - \frac{\zeta}{\pi^2} \int_{t=1}^{b} \frac{\gamma_s(t)\Lambda(t)dt}{t^2 - \zeta^2} \right] \right\} \tag{A21}$$

with

$$\Lambda(\zeta) \equiv \int_{\zeta_0=-1}^{1} \frac{\cos \widetilde{\beta}(\zeta_0)d\zeta_0}{\chi(\zeta_0)(\zeta - \zeta_0)}. \tag{A22}$$

Integration order interchange has been allowed in the reduction to (A22) in view of the non-overlapping t and ζ_0 ranges.

Although not a commonly encountered integral, (A22), for continuous but otherwise arbitrary $\kappa(s)$, is:

$$\Lambda(s) = \begin{cases} \pi \left(-s + \frac{\sqrt{1-s^2}\sin \widetilde{\beta}(s)}{\kappa(s)} \right) & s \leq 1 \\[3mm] \pi \left(-s + \frac{\sqrt{s^2-1}}{\kappa(s)} \right) & s > 1 \end{cases} \tag{A23}$$

Substitution of (A19) and (A23) into (A21) produces:

$$\gamma_c(\zeta) = -\frac{2 \cos \widetilde{\beta}(\zeta)\zeta\kappa(\zeta)}{\sqrt{1-\zeta^2}} \left[V + \frac{1}{\pi} \int_{t=1}^{b} \frac{\gamma_s(t)\sqrt{t^2-1}dt}{\kappa(t)(t^2 - \zeta^2)} \right] \tag{A24}$$

This is the general result applied the text, which can be seen in the rigid cylinder terms of Equation (15).

References

1. T. Von Kármán, The impact of seaplane floats during landing. Technical Note 321, NACA, Washington, D.C. (1929).
2. H. Wagner, Über Stoss-und Gleitvorgänge an der Oberfläche von Flüssigkeiten. *ZAMM* 12 (1932) 193–215.
3. W.S. Vorus, A flat cylinder theory for vessel impact and steady planning resistance. *J Ship Res* 40 (1996) 89–106.
4. D.J. Kim, W.S. Vorus, A.W. Troesch and R.M. Gollwitzer, Coupled hydrodynamic impact and elastic response. In: E. Rood (ed.), Proc. 21st *Symposium on Naval Hydrodynamics*. Office of Naval Research, Oslo, Norway. June (1996) pp. 424–437.

5. L.A. Xu, A.W. Troesch and W.S. Vorus, Asymmetric vessel impact and planing Hydrodynamics. *J Ship Res.* 42 (1998) 187–198.
6. J.P. Breslin, Chines-dry planing of slender hulls: a general theory applied to prismatic surfaces. *J. Ship Res.* 45 (2001) 59–72.
7. B.R. Savander, S.M. Scorpio and R.K. Taylor, Steady hydrodynamic analysis of planing surfaces. *J. Ship Res.* 46 (2002) 248–279.
8. Z. Zhou, *A Theory and Analysis of Planing Catamarans in Calm and Rough Water.* School of NAME, University of New Orleans, PhD Thesis (2003) 407 pp.
9. W.S. Vorus and R.A. Royce, Wave impact reduction of planing boats. Ship Structures Symposium 2000, SNAME, Washington, D.C., June (2000) pp. 1–14.
10. R. Cointe and J-L. Armand, Hydrodynamic impact analysis of a cylinder. *J. Offshore Mech. and Arctic Engng.* 109 (1987) 237–243.
11. S.D. Howison, J.R. Ockendon, and S.K. Wilson, Incompressible water entry problems at small deadrise angles. *J. Fluid Mech.* 222 (1991) 215–230.
12. R. Zhao and O.M. Faltinsen, Water entry of two-dimensional bodies. *J. Fluid Mech.* 246 (1993) 593–612.
13. N.L. Mushkhelishvili, *Singular Integral Equations*. Leyden: Noordhoff International Publishing (1958) 447 pp. (also Dover reprint).
14. I.S. Gradshteyn and I.M. Ryzhik, *Table of Integrals, Series, and Products*. New York: Academic Press (1965) 1086 pp.
15. S. Ando, Cushoning of slamming by elastomeric layers. *J. Ship Res.* 33 (1989) 169–175.
16. F.G. Tricomi, *Integral Equations*. New York: Interscience (1957) 238 pp.